

Single-Molecule Studies

Cryogenic Correlative Single-Particle Photoluminescence Spectroscopy and Electron Tomography for Investigation of Nanomaterials

 Peter D. Dahlberg⁺, Davis Perez⁺, Zhaoming Su, Wah Chiu, and W. E. Moerner*

Abstract: Cryogenic single-particle photoluminescence (PL) spectroscopy has been used with great success to directly observe the heterogeneous photophysical states present in a population of luminescent particles. Cryogenic electron tomography provides complementary nanometer scale structural information to PL spectroscopy, but the two techniques have not been correlated due to technical challenges. Here, we present a method for correlating single-particle information from these two powerful microscopy modalities. We simultaneously observe PL brightness, emission spectrum, and in-plane excitation dipole orientation of CdSSe/ZnS quantum dots suspended in vitreous ice. Stable and fluctuating emitters were observed, as well as a surprising splitting of the PL spectrum into two bands with an average energy separation of 80 meV. In some cases, the onset of the splitting corresponded to changes in the in-plane excitation dipole orientation. These dynamics were assigned to structures of individual quantum dots and the excitation dipoles were visualized in the context of structural features.

Introduction

A goal of many semiconductor quantum dot syntheses is a homogeneous batch of particles.^[1] The more homogeneous the preparation, the easier it is to use particles reliably and to correlate photophysical properties to structural features. However, there will always be some degree of heterogeneity in the particles produced, both in structure and in optical properties. Here we describe a new approach, cryogenic correlative single-particle photoluminescence spectroscopy and electron tomography which can cut through photophysical and structural heterogeneity by recording PL properties of individual quantum dots and correlating these properties with their corresponding three-dimensional reconstructions determined by cryogenic electron tomography (cryo-ET).

How to cite: *Angew. Chem. Int. Ed.* **2020**, *59*, 15642–15648
 International Edition: doi.org/10.1002/anie.202002856
 German Edition: doi.org/10.1002/ange.202002856

This approach provides insight into the electronic structure, physical structure, and environment of single quantum dots, and allows for the observation of heterogeneity that is lost in an ensemble-averaged measurement, but is retained in single-molecule spectroscopy.^[2]

Performing single-particle optical microscopy experiments at cryogenic temperatures comes with a number of benefits over room-temperature experiments. For example, cryogenic temperatures produce PL line narrowing,^[3–5] which improves spectral resolution, and cryogenic temperatures reduce the quantum yield of photobleaching,^[6] which increases the total number of photons that can be collected. The spatial resolution of optical microscopy is restricted by the Abbe diffraction limit to about half the wavelength of emitted light. While this can be improved by single-molecule localization techniques,^[7] especially at cryogenic temperatures,^[8,9] PL alone can never resolve the nanoscale physical structure of individual emitters in far-field microscopy due to its detection by electric-dipole radiation. Cryo-ET is a complementary technique to single-molecule PL spectroscopy as it provides excellent spatial resolution, but no information about the corresponding electronic structure. The combination of these two powerful approaches allows for the correlation of physical and electronic structure of individual emitters and can lead to insight inaccessible by either technique independently.

In this work, we chose to apply this new correlative method to commercially available CdSSe/ZnS semiconductor nanocrystals or quantum dots (QDs). Because of their tunable band gaps, large quantum yields, and robust synthesis methods,^[10] QDs are promising for many potential device applications.^[11] However, it is well known that their performance in many of these applications is limited by PL intermittency (blinking) and spectral diffusion, both of which can only be observed at the single particle level.^[12,13]



PL blinking was first observed in quantum dots in 1996,^[13] and has since been a topic of considerable study.^[14–16] It is generally attributed, at least in part, to trapped charges causing large local electric fields, driving non-radiative Auger recombination.^[17] Explanations involving multiple recombination centers,^[18] surface vacancies,^[19] or combinations of the above have also been proposed.^[20] Blinking has been shown to follow power law statistics and is found to be dependent on many experimental parameters such as excitation wavelength and intensity, environment, and core/shell composition and thickness.^[17,21,22] More recent studies have found the existence of one or multiple emissive states with intermediate brightness, complicating the simple on/off picture. These “grey” states have been shown to exhibit different lifetimes,^[23,24] and have been attributed to a positive or negative trion state.^[25]

[*] Dr. P. D. Dahlberg,^[†] D. Perez,^[†] Prof. W. E. Moerner
 Department of Chemistry, Stanford University
 Stanford, CA 94305 (USA)
 E-mail: wmoerner@stanford.edu

Dr. Z. Su, Prof. W. Chiu
 Department of Bioengineering, Stanford University
 Stanford, CA 94305 (USA)

Prof. W. Chiu
 Division of CryoEM and Bioimaging, SSRL
 SLAC National Accelerator Laboratory
 Menlo Park, CA 94025 (USA)

[†] These authors contributed equally to this work.

 Supporting information and the ORCID identification number(s) for the author(s) of this article can be found under:
 <https://doi.org/10.1002/anie.202002856>.

Spectral diffusion of single QDs has a similarly long history of study, both at low temperatures^[26] and above room temperature.^[27] Large shifts have been attributed to the quantum confined Stark effect caused by electric fields created by trapped charges.^[28] This excess charge can result in local electric fields on the order of tens of MV cm^{-1} , which can cause spectral shifts on the order of tens to hundreds of meV .^[17,28] These spectral shifts have since been correlated with PL blinking.^[29]

Comparative studies of spectroscopic and structural properties conducted on the same batch of QD nanoparticles have yielded insights.^[30–32] However, most PL studies of single quantum dots have not correlated the physical structure and orientation of each specific QD or cluster of QDs that gives rise to the observed spectrum and blinking dynamics. A few studies have correlated the physical structure of individual QDs with some details of their PL, yielding interesting observations. For example, recent work has shown a relationship between quantity and location of surface defects and PL efficiencies in quantum dot-in-rod nanostructures.^[33] Similarly, the PL emission polarization of single quantum dots was matched to high-resolution room-temperature transmission electron microscope (TEM) images of the same quantum dot.^[34] When super-resolution techniques were combined with scanning electron microscopy of clusters of QDs, the center of the emission was observed to shift as the PL intensity changed.^[35] This method can be used to map energy flow through a nanoscopic system. While these studies provide novel insights into the correlated structure and PL of individual and clusters of QDs, our new approach extends these measurements by combining PL spectroscopy at cryogenic temperatures and state of the art cryogenic electron microscopy. Here, we demonstrate correlation of in-plane excitation dipole, PL intensity, and PL spectra with three dimensional cryo-ET reconstructions of individual QDs. Additionally, we observe unreported dynamic PL spectral splitting on the order of 80 meV in CdSSe/ZnS core-shell quantum dots suspended in vitreous ice.

Commercially available CdSSe/ZnS QDs, characterized by room-temperature TEM and bulk PL spectroscopy (see Figure S1), were dissolved in nanopure water and plunge frozen on SiO_2 finder grids. This preparation resulted in a dilute sample of quantum dots suspended in a thin layer of vitreous ice. The plunge frozen sample was then loaded into a cryogenic microscope stage on a home-built widefield fluorescence microscope^[36] outlined in Figure 1 b. The sample was excited by a 594 nm laser whose polarization was varied each imaging frame in approximately 60 degree steps to recover the in-plane projection of the excitation dipole orientation.^[37] For more details on the PL spectroscopy see the Experimental Section of the Supporting Information.

While organic dye molecules generally have single electric dipole transitions, QDs have numerous transition dipoles, some of which form a two-dimensional plane due to degeneracies.^[34,38] This two-dimensional plane of dipoles is often referred to as the “bright” plane, and it is the projection of this bright plane and other transition dipoles onto the sample plane to which our method is sensitive. By observing the change in detected PL intensity over our three linear

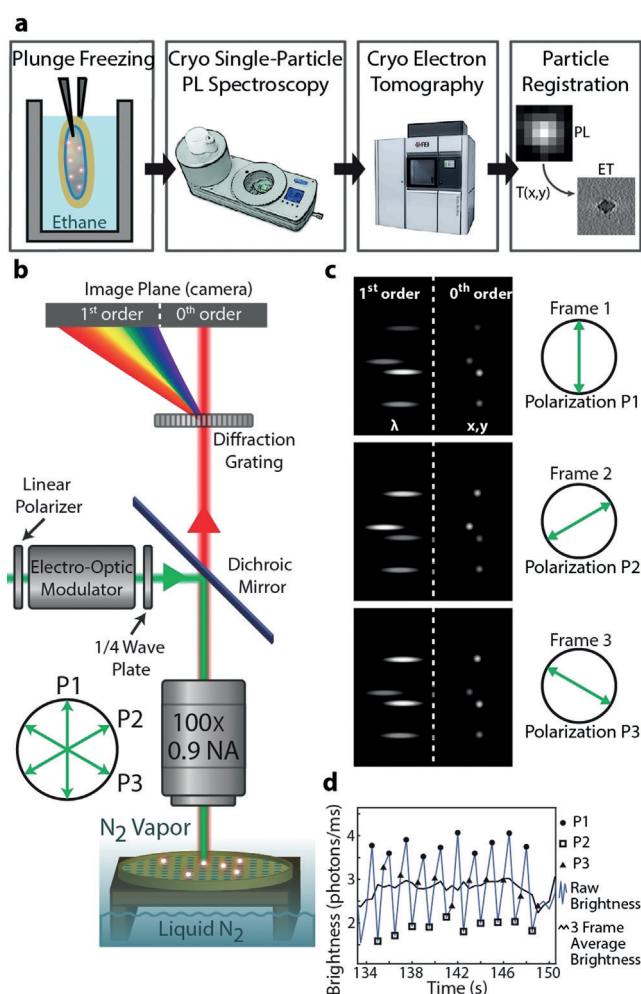


Figure 1. Overview of experiment. a) Outline of experimental workflow. Samples are plunge frozen to suspend QDs in vitreous ice, then fluorescently imaged. Cryo-ET is then conducted at 77 K on the same sample, and the images are registered. b) Schematic of home-built cryogenic widefield fluorescence microscope. The excitation laser is passed through a linear polarizer, an electro-optic modulator (EOM) and a quarter wave plate to produce excitation polarization modulated every frame (500 ms) in $\approx 60^\circ$ steps. Emission is dispersed onto an EMCCD camera by a diffraction grating. c) Illustration of separation of position and spectral information on the EMCCD and change in brightness with changing excitation polarization. Different emitters show different response to excitation polarization based on their preferred in-plane excitation dipole orientation. d) Example brightness trace for a single QD. In blue is the raw trace showing the three-frame periodic change in brightness due to the stepped excitation polarization. Frames at polarizations P1, P2, and P3 are marked with circles, empty squares, and triangles, respectively. A three-frame moving average brightness is plotted in black to more clearly show changes in brightness not associated with changes in excitation polarization.

pumping polarizations, the preferred in-plane excitation dipole orientation can be determined for each emitter in the field of view, see Supporting Information for analysis details. An example of the three-frame periodic fluctuation of PL brightness is plotted along with a three-frame moving average in Figure 1 d. Emission from the sample is spectrally resolved on an EMCCD camera following transmission through a diffraction grating,^[39] allowing for simultaneous determi-

nation of the emitter location and PL spectrum in the 0th and 1st order spots, respectively, as shown in Figure 1c. The Supplementary Video S1 shows an example of raw fluorescence data following post-processing drift correction.

The same grid that was imaged in fluorescence is loaded into a 200 keV electron microscope (Talos Arctica, Thermo Fisher Scientific). Using the finder grid, the grid square location measured on the fluorescence microscope is easily identified. Then, using the unique pattern of holes that are filled with vitreous ice, a rough registration can be performed by eye (see Figure S2). The individual QD's and clusters of QD's that were imaged in fluorescence can then be identified in low magnification electron micrographs. Following this identification, tomograms of the dots/clusters of interest were acquired. Due to the robustness of the QDs the total electron dose for the sample was 1000 e⁻ Å⁻² or ≈12 times higher than that typically used for biological samples. Three-dimensional tomographic reconstructions of the QDs were performed using IMOD's ETOMO package^[40] and the resulting reconstructions were annotated using the neural net from EMAN2^[41] and visualized in Chimera.^[42]

Post-acquisition, a fine alignment between the images taken in the light microscope and a low magnification electron micrograph is performed using the manually identified centers of the holes in the SiO₂ substrate as control point pairs for a projective transformation. Subsequent higher magnification electron micrographs can then be easily aligned to the lower magnification micrographs, see Figure S2 for a more detailed description of the registration process. The overall result of this alignment is a correlation of the dynamic PL spectra, brightness and in-plane excitation dipole to the three-dimensional cryo-ET reconstruction. In total, cryogenic PL data was collected for 93 individual or clusters of quantum dots, 18 of which were correlated with cryo-ET tomograms. Ten of these 18 were found to be single QDs from the cryo-ET, while the other eight were clusters of several QDs.

Results and Discussion

Figure 2 shows an example of one of the correlations that identified a cluster of quantum dots via electron microscopy. While the emission from a cluster of QDs (Figure 2a) hinders the ability of our method to extract excitation dipole orientation and emission spectra corresponding to individual emitters, the observation of clusters of emitters does highlight the ability to register super-localizations with ground truth localizations provided by electron microscopy. We now analyze the results in detail.

As is well-known, one challenge in localizing individual emitters is isolating the contributions from individual emitters in the presence of overlapping point spread functions (PSFs). In order to overcome this challenge, fluctuations in the integrated intensity corresponding to a cluster of QDs were analyzed and large single-step changes in intensity arising from a “blinking” or “bleaching” event can be reasonably attributed to an individual QD within the cluster (see Figure 2b). Frames adjacent in time to the “blinking” or “bleaching” event that were of a consistent intensity level

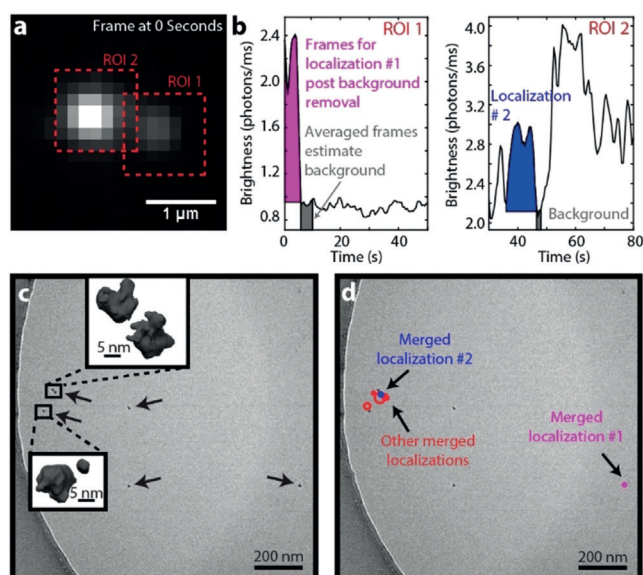


Figure 2. Overlay of single-QD emission localizations and electron microscopy data. a) Cropped region of a frame showing the 0th order spots generated by two spatially separated emitters. b) Intensity of the integrated areas shown as dashed red boxes in (a) as a function of time. In the rare cases where there is substantial overlap of the point spread functions from several emitters, as is the case for ROI 2, the contributions from individual emitters can be isolated by subtracting the average of frames adjacent in time to large intensity changes from blinking. The large signals (magenta and blue) above the estimated background (gray) can then be attributed to an individual emitter. c) Medium magnification electron micrograph corresponding to the area shown in (a). Black arrows highlight the location of quantum dots. Inset shows the three-dimensional reconstruction from higher magnification cryo-ET. d) Overlay of merged localizations shown as red circles. Magenta and blue circles correspond to the localizations from (b). The radius of the circles is the localization precision estimated by the standard error of the mean of the individual frame localizations.

were averaged and used as an estimate of the background corresponding to the overlapping PSFs underlying the single emitter. Following removal of this background, the remaining intensity is attributed to the individual dot that has undergone the “blinking” or “bleaching” and can be used to localize the dot.^[43,44] Each consecutive frame where an individual emitter's intensity can be isolated and localized provides an estimate of that emitter's position, in this case by fitting the remaining PSF to a symmetric Gaussian.^[45] In the 3D tomogram, we can visualize the high density QD as in Figure 2c. Each of these single-frame estimates should then be merged into a single localization with a precision provided by the standard error on the mean of the individual frame localizations (see Figure 2d). Next, we analyze PL dynamics that can be assigned to individual QDs and not clusters.

The PL data for three single QDs are shown in Figure 3 and their corresponding medium magnification micrographs are shown in Figure S3. For each QD, the PL brightness, spectrum, and preferred in-plane excitation dipole orientation are plotted as functions of time. Note that for the brightness traces and spectra, three-frame moving averages are plotted to portray changes not associated with the periodic change in excitation polarization. PL brightness

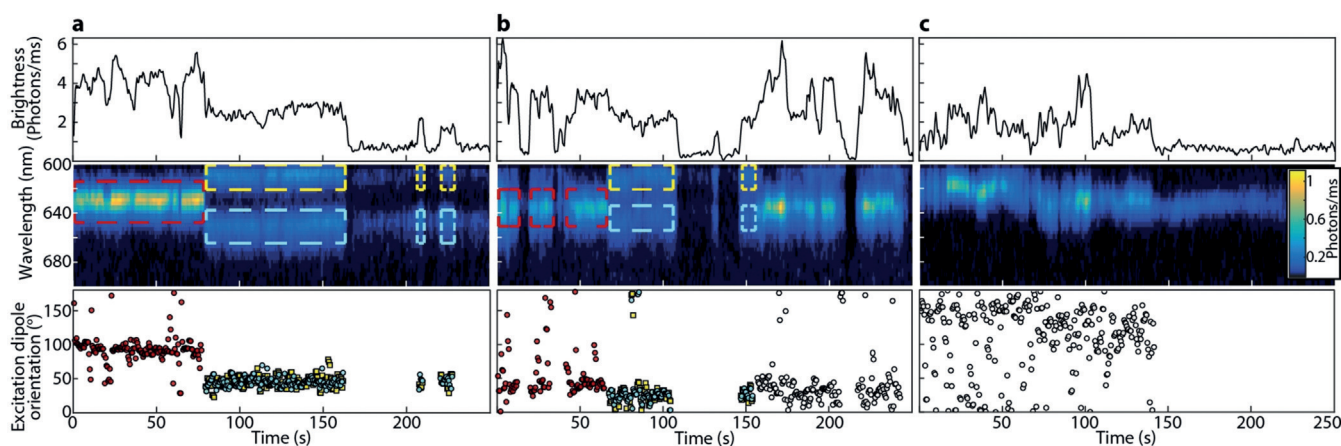


Figure 3. PL data for single QDs. For (a), (b) and (c), the top panel shows a three-frame running average of the brightness extracted from the 0th order image scaled by 5.8 to represent photons collected in both the 0th and 1st order images. The middle panels show a waterfall plot of the spectra extracted from the 1st order image over time, also averaged over three frames. The smoothing is done to show changes in brightness not associated with changes in the excitation polarization. The bottom panel shows the in-plane excitation dipole orientation calculated for each frame from the current brightness and the brightness of the next two frames. Red circles, blue circles, and yellow squares show orientation calculated from brightness extracted from the spectral regions boxed in red, blue, and yellow, respectively. Orientations marked with white circles are calculated from the brightness in the 0th order spot over three consecutive frames.

was extracted from the 0th order image then scaled by an experimentally determined calibration factor to quantify photons collected in both the 0th and 1st order spots. Spectra were collected from the 1st order image. Preferred in-plane excitation dipole orientation was calculated from specific spectral regions by analyzing the number of photons collected in a given spectral region in each frame as a function of time and excitation polarization.

The PL data of these QDs display several notable features. In both Figure 3 a and b, the QDs exhibit a change in intensity associated with a surprising transition from a single peaked spectrum to a split spectrum and a change in preferred excitation dipole orientation. The PL for the QD presented in Figure 3 a starts with a single peak centered at 630.4 ± 0.1 nm with an average brightness of 4.06 ± 0.08 photons ms^{-1} . The preferred in-plane dipole orientation, calculated from the region around the spectrum denoted by the red box, was centered around 93° relative to an arbitrary fixed axis in the sample plane. This state lasted for 79 seconds, after which the average brightness dropped to 2.52 ± 0.06 photons ms^{-1} and the spectrum exhibited a dramatic split to two peaks centered at 609.34 ± 0.08 nm and 650.3 ± 0.1 nm. The distance between these peaks, which we will call the splitting energy, was 128.2 ± 0.3 meV. Notably both spectral regions in the split state showed the same preferred excitation dipole orientation of 46° (see overlapping blue and yellow symbols). This state persisted for 85 seconds. While the recovered in-plane excitation dipoles are often quite consistent, the preference is fairly weak (see Figure S4 and Supporting Information). The QD then entered a dim state, while the spectrum remained split with peaks at approximately the same wavelengths. The signal to noise ratio during this dim emission period was too low to calculate dipole orientation, but 45 seconds later, the QD returned to a bright state for two shorter periods with brightness slightly lower than the previous intermediate state. The preferred in-plane

excitation dipole orientation was the same as the earlier split state, but both emission peaks appeared slightly blue shifted (2–4 nm). This suggests that the two states observed at 208 and 221 seconds are similar but not identical to the longer-lived split state.

Figure 3 b shows another example of PL data for a single QD. Once again the emission starts as a single peak. In this case the emission is more intermittent, with the QD blinking off for two short periods and returning to the same single peaked state. Average brightness and peak emission over these three periods are 3.4 ± 0.1 photons ms^{-1} and 635.7 ± 0.6 nm, respectively, with a preferred in-plane excitation dipole orientation of 41° . After 67 seconds, the spectrum splits into two peaks, again with a corresponding decrease in brightness and a change in excitation dipole orientation. In this case the splitting in energy was smaller, with an average gap of 105 ± 1 meV, and less symmetric about the single initial peak, with emission peaks centered around 611.3 ± 0.3 and 644.7 ± 0.5 nm. The difference in in-plane excitation dipole orientation is also smaller, with a change of about 19° . The QD then enters a very dim state, interrupted by a brief return to the split emissive state. When the emission returns at 147 seconds, the brightness and peaks are comparable to the previous split state, but the in-plane excitation dipole orientation is different by about 5° .

From 159 seconds on to the end of the acquisition time, the QD appears to sample many states with different brightness levels and emission spectra. For some periods it appears to be similar to the prolonged single peaked state at the beginning of the trace, but most states are too short lived to be effectively characterized. Throughout this time, the excitation dipole appears to sample various angles between those angles observed in the single peaked and split states. Another notable feature is the appearance of what looks to be the shoulder of a peak close to 600 nm beginning around 175 seconds. Due to the filters used in this experiment,

emission to the blue of 600 cannot be resolved and so this peak cannot be effectively quantified, but it appears to be very close to the excitation wavelength of 594 nm. These two QDs display two of the largest splits and orientation changes of our sample set, but these behaviors are observed in many of the PL measurements to varying degrees.

While splitting is not observed in Figure 3c, this single QD is representative of many of the wandering behaviors observed in this experiment. For the first 70 seconds, emission is loosely centered on 620 nm, and the QD exhibits multiple changes in brightness. It is important to note that the orientation calculation is sensitive to changes in brightness unrelated to change in excitation polarization occurring during the three-frame window from which the excitation polarization is calculated. Therefore, orientations (such as the many isolated measurements between 10° and 100° in the Figure) should not be considered physically meaningful unless numerous adjacent measurements show similar orientations and brightness. During these first 70 seconds the preferred in-plane excitation dipole orientation varies widely in part due to fluctuations in brightness, but maintains a consistent average value of 160° . The emission then redshifts to 632.9 ± 0.7 nm accompanied with a change in preferred in-plane excitation dipole orientation to 130° . Then, from 150 to 250 seconds, the dot becomes very dim (0.66 ± 0.02 photons ms^{-1}) and signal to noise is too low to calculate excitation dipole orientation.

Overall, these examples portray much of the dynamic intensity and spectral data we observed in all of the single dots we examined. PL data for additional single QDs observed in this experiment is presented in Figure S5. While we have referred to the PL dynamics in Figure 3 as arising from single QDs, the PL data alone does not justify this assignment. Quite to the contrary, the numerous brightness levels, excitation dipoles, and emission bands observed in the PL would naively indicate a complex cluster of QDs rather than an isolated dot. Often to determine if emission comes from a single emitter, photon antibunching or the $g^{(2)}$ function is measured.^[46] However, this requires photon arrival time information that is not easily collected in a wide field imaging setup. Here, it is only with the correlative tomography data that we are able to definitively assign these dynamics to individual QDs. This correlation also permits the interpretation of the PL data within the context of the three-dimensional structure provided by cryo-ET. Figure 4 and Supplementary Video S2 show the overlay of several recovered in-plane excitation dipoles with their corresponding three-dimensional cryo-ET reconstructions.

The single dot structures shown in Figure 4a and b correspond to the PL data shown in Figure 3a and b, respectively, where the arrows show the different excitation dipoles measured. Figure 4c shows a pair of QDs that are close together, ≈ 13 nm between the centers of mass. This pair exhibited a slightly preferred and short-lived excitation axis corresponding to the period of brightest emission (see Figure S6). This preferred excitation dipole could be due to electronic coupling between the two dots and is closely aligned with the line joining the two centers of mass in the x - y plane shown in black. Due to the limited sample size of

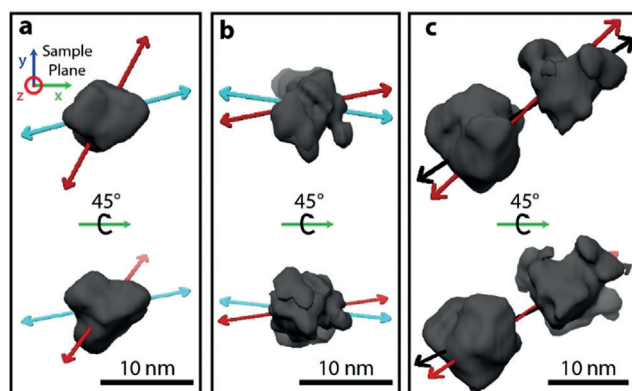


Figure 4. Correlation of PL orientation measurements and cryo-ET reconstructions. The upper images are a top down view, and the lower images are rotated 45° around horizontal. a) Overlay of cryo-ET reconstructions (gray) and the excitation dipoles (red and cyan arrows) corresponding to the red and cyan boxes from Figure 3a. b) Same as (a) except arrows and structure correspond to fluorescence data from Figure 3b. c) A pair of dots that was observed to have a weak preference for excitation along the red arrow which aligns closely with the black line joining the centers of mass in xy plane.

single QDs that display a change in in-plane excitation dipole orientation upon transition from single to split peaked spectra, no clear correlation between structural features and excitation dipoles can be determined with confidence. However, these overlays demonstrate the power of this technique by definitively assigning these complex dynamics to single QDs and in the case of the QD pair by displaying the suggestive alignment between the physical vector joining the QDs and the weak in-plane dipole preference.

With the clear assignment of the spectral splitting arising from single QDs demonstrated by our correlative approach, we next characterize this splitting phenomenon. While the correlative data is limited to just 18 examples of single QDs and clusters, PL data was collected for 93 luminescent objects. Twenty six of the 93 objects display some degree of spectral splitting. Figure 5a shows a histogram of splitting energies observed in the full PL dataset plotted with markers denoting the splitting energies of single QDs verified by associated cryo-ET data. Inspection of this histogram shows the smaller set of correlated singles effectively samples from the larger population. Figure 5b–d show time averaged spectra of single-peaked and split states for three individual QDs. The spectra in Figure 5b correspond to the QD in Figure 3a and 4a. This QD displayed the largest splitting energy. Likewise, the spectra in Figure 5c correspond to the PL data in Figure 3b and the three-dimensional reconstruction shown in Figure 4b. The split spectrum from another single QD shown in Figure 5d displayed the smallest splitting energy.

To our knowledge, this is the first reported observation of this spectrally split emission behavior at the single QD level. This is likely due to several unique aspects of our experiment. Most notably, the environment surrounding the quantum dots is vitreous ice. Traditionally both room temperature and cryogenic single-particle QD studies have been conducted on QD suspend in a thin polymer surface or on bare glass, either in vacuum or under a range of different gasses. To explore the

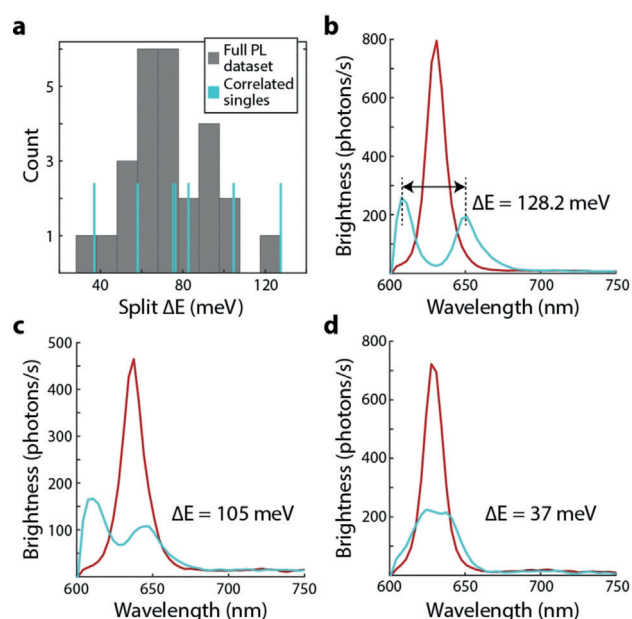


Figure 5. a) Histogram of observed splitting energies in meV. Splitting energy is defined as the average energy difference between the center of two Gaussian functions fit to the split emission spectra. In cyan are the average splitting energies of each of the seven single QDs with correlated three-dimensional structure that exhibited split emission spectra. In grey are the average splitting energies of all objects that exhibited split emission spectra regardless of correlative data. b–d) Time-averaged spectrum from boxed time windows of the split and single-peaked state for the QD in b) Figure 3 a and 4 b c) Figure 3 b and 4 b, and d) Figure S5b.

impact of the local environment on the splitting phenomenon, the 77 K PL spectroscopy component of the experiment was repeated for QDs under three different preparations: 1) spun coat on bare coverslips, 2) spun coat in poly(vinyl alcohol–vinyl acetate) (PVA-VA) on coverslips and dried, and 3) frozen in polycrystalline ice. For the bare glass samples only one case of possible spectral splitting was observed in 70 total spectra, and one in 14 for the PVA-VA samples. The polycrystalline ice samples, in contrast, exhibited spectral splitting in 22 out of 90 of the observed objects. This rate is similar to that observed in vitreous ice, and suggests the unique nature in which the sample is frozen is not the cause of this behavior, but the details of the host environment are important.

While definitive assignment of the mechanism leading to split emission is beyond the scope of this work demonstrating cryogenic correlative imaging, the phenomenon is likely due to charged states or free charges. This suggestion is in large part due to the magnitude of the energy splitting observed. While fine splitting of QD emission has been reported from states where a degeneracy has been lifted by a variety of means such as an external magnetic field, excitation polarization, or structural asymmetry, the energy differences due to these effects are typically on the order of μeV to a few meV ^[47–50] and are inconsistent with our observations. One possible explanation may be that after continued illumination some QDs acquire a net charge of two electrons. Previous work conducted on CdSe QDs attached to an electrode in an

electrochemical cell showed that when each QD has a charge of two electrons, filling the $1S_e$ state, the PL spectrum has two peaks with emission coming either from the S^{2-} exciton or the P^{2-} exciton with similar probabilities. The P^{2-} recombination is blue shifted from the S recombination, while the S^{2-} emission is red-shifted due to the Stark effect^[51] (see Figure S7). It is possible that in our experiments, where no external field is applied to the QDs, the ice environment serves to more effectively stabilize doubly charged QDs which would otherwise not exist for appreciable amounts of time. Another possibility is that we are observing changes in the emission spectrum upon the formation of a trion state. The decreased brightness observed here upon the transition to the split emission is consistent with previous changes in brightness attributed to trion formation,^[24] though how a trion state could lead to two distinct emission bands is unclear. Further work is needed to assign a mechanism that gives rise to these split emission features for single QDs.

Conclusion

In summary, we have developed a method to correlate detailed single-particle PL spectroscopic measurements including brightness, position, spectra, and in-plane excitation dipole with 3D nanometer-scale reconstructions from cryo-ET. By applying this technique to commercially available CdSSe/ZnS quantum dots trapped in vitreous ice at cryogenic temperatures, we observed a previously unreported dynamic PL spectral splitting phenomenon at the single QD level. With high spatial resolution information from cryo-ET we can definitively assign PL data to specific single QDs. By employing our image registration technique, we were able to visualize the dynamically changing in-plane excitation dipole orientation overlaid on a three-dimensional reconstruction of the QD. Because this method investigates samples suspended in vitreous ice, it is generalizable to fragile nanomaterial systems and biological systems not accessible by correlative imaging techniques at room temperature.

Acknowledgements

This material is based upon work supported in part by the U.S. Department of Energy, Office of Science, Office of Basic Energy Sciences, Chemical Sciences, Geosciences, & Biosciences Division, under Award DE-FG02-07ER15892 (Physical Biosciences Program). D.P. is supported as a Stanford Graduate Fellow. The JEOL JEM1400 transmission electron microscope used for room-temperature characterization and preliminary experiments was funded by NIH Grant 1S10RR02678001 to the Stanford Microscopy Facility. Cryogenic Electron Tomography performed at the Stanford Linear Accelerator was supported by the National Institute of General Medical Sciences Grant No. P41GM103832. We thank A. P. Alivisatos for helpful discussion.

Conflict of interest

The authors declare no conflict of interest.

Keywords: correlative light electron microscopy (CLEM) · cryogenic electron tomography · fluorescence spectroscopy · nanoparticles · single-molecule studies

- [1] C. B. Murray, C. R. Kagan, M. G. Bawendi, *Annu. Rev. Mater. Sci.* **2000**, *30*, 545–610.
- [2] W. E. Moerner, L. Kador, *Phys. Rev. Lett.* **1989**, *62*, 2535–2538.
- [3] R. I. Personov, E. I. Al'Shits, L. A. Bykovskaya, *Opt. Commun.* **1972**, *6*, 169–173.
- [4] S. Empedocles, M. Bawendi, *Acc. Chem. Res.* **1999**, *32*, 389–396.
- [5] A. V. Naumov, *Phys.-Usp.* **2013**, *56*, 605–622.
- [6] C. N. Hulleman, W. Li, I. Gregor, B. Rieger, J. Enderlein, *ChemPhysChem* **2018**, *19*, 1774–1780.
- [7] W. E. Moerner, *Nat. Methods* **2006**, *3*, 781–782.
- [8] S. Weisenburger, D. Boening, B. Schomburg, K. Giller, S. Becker, C. Griesinger, V. Sandoghdar, *Nat. Methods* **2017**, *14*, 141.
- [9] S. Weisenburger, B. Jing, D. Hänni, L. Reymond, B. Schuler, A. Renn, V. Sandoghdar, *ChemPhysChem* **2014**, *15*, 763–770.
- [10] A. P. Alivisatos, *J. Phys. Chem.* **1996**, *100*, 13226–13239.
- [11] J. M. Pietryga, Y. Park, J. Lim, A. F. Fidler, W. K. Bae, S. Brovelli, V. I. Klimov, *Chem. Rev.* **2016**, *116*, 10513–10622.
- [12] S. A. Empedocles, D. J. Norris, M. G. Bawendi, *Phys. Rev. Lett.* **1996**, *77*, 3873–3876.
- [13] M. Nirmal, B. O. Dabbousi, M. G. Bawendi, J. J. Macklin, J. K. Trautman, T. D. Harris, L. E. Brus, *Nature* **1996**, *383*, 802–804.
- [14] R. Verberk, A. M. van Oijen, M. Orrit, *Phys. Rev. B* **2002**, *66*, 233202.
- [15] S. Hohng, T. Ha, *J. Am. Chem. Soc.* **2004**, *126*, 1324–1325.
- [16] G. Yuan, D. E. Gómez, N. Kirkwood, K. Boldt, P. Mulvaney, *ACS Nano* **2018**, *12*, 3397–3405.
- [17] A. L. Efros, D. J. Nesbitt, *Nat. Nanotechnol.* **2016**, *11*, 661–671.
- [18] P. A. Frantsuzov, S. Volkán-Kacsó, B. Jankó, *Phys. Rev. Lett.* **2009**, *103*, 207402.
- [19] O. Voznyy, E. Sargent, *Phys. Rev. Lett.* **2014**, *112*, 157401.
- [20] I. S. Osad'ko, I. Y. Eremchev, A. V. Naumov, *J. Phys. Chem. C* **2015**, *119*, 22646–22652.
- [21] M. Kuno, D. P. Fromm, H. F. Hamann, A. Gallagher, D. J. Nesbitt, *J. Chem. Phys.* **2001**, *115*, 1028–1040.
- [22] K. Goushi, T. Yamada, A. Otomo, *J. Phys. Chem. C* **2009**, *113*, 20161–20168.
- [23] P. P. Jha, P. Guyot-Sionnest, *ACS Nano* **2009**, *3*, 1011–1015.
- [24] F. Gao, P. Bajwa, A. Nguyen, C. D. Heyes, *ACS Nano* **2017**, *11*, 2905–2916.
- [25] Y. Park, W. K. Bae, J. M. Pietryga, V. I. Klimov, *ACS Nano* **2014**, *8*, 7288–7296.
- [26] T. Plakhotnik, M. J. Fernee, B. Littleton, H. Rubinsztein-Dunlop, C. Potzner, P. Mulvaney, *Phys. Rev. Lett.* **2010**, *105*, 167402.
- [27] E. A. Podshivaylov, M. A. Kniazeva, A. A. Gorshchev, I. Y. Eremchev, A. V. Naumov, P. A. Frantsuzov, *J. Chem. Phys.* **2019**, *151*, 174710.
- [28] S. A. Empedocles, M. G. Bawendi, *Science* **1997**, *278*, 2114–2117.
- [29] R. G. Neuhauser, K. T. Shimizu, W. K. Woo, S. A. Empedocles, M. G. Bawendi, *Phys. Rev. Lett.* **2000**, *85*, 3301–3304.
- [30] J. Cui, Y. E. Panfil, S. Koley, D. Shamalia, N. Waikopf, S. Remennik, I. Popov, M. Oded, U. Banin, *Nat. Commun.* **2019**, *10*, 5401.
- [31] T. Fischer, S. Stöttinger, G. Hinze, A. Bottin, N. Hu, T. Basché, *Nano Lett.* **2017**, *17*, 1559–1563.
- [32] K. R. Karimullin, A. I. Arzhanov, I. Y. Eremchev, B. A. Kulnitskiy, N. V. Surovtsev, A. V. Naumov, *Laser Phys.* **2019**, *29*, 124009.
- [33] K. R. Reid, J. R. McBride, A. D. La Croix, N. J. Freymeyer, S. M. Click, J. E. Macdonald, S. J. Rosenthal, *ACS Nano* **2018**, *12*, 11434–11445.
- [34] F. Koberling, U. Kolb, G. Philipp, I. Potapova, T. Basché, A. Mews, *J. Phys. Chem. B* **2003**, *107*, 7463–7471.
- [35] D. P. Ryan, P. M. Goodwin, C. J. Sheehan, K. J. Whitcomb, M. P. Gelfand, A. Van Orden, *J. Phys. Chem. C* **2018**, *122*, 4046–4053.
- [36] P. D. Dahlberg, A. M. Sartor, J. Wang, S. Saurabh, L. Shapiro, W. E. Moerner, *J. Am. Chem. Soc.* **2018**, *140*, 12310–12313.
- [37] A. S. Backer, M. Y. Lee, W. E. Moerner, *Optica* **2016**, *3*, 659.
- [38] S. A. Empedocles, R. Neuhauser, M. G. Bawendi, *Nature* **1999**, *399*, 126–130.
- [39] M. N. Bongiovanni, J. Godet, M. H. Horrocks, L. Tosatto, A. R. Carr, D. C. Wirthensohn, R. T. Ranasinghe, J. Lee, A. Ponjavic, J. V. Fritz, C. M. Dobson, D. Klenerman, S. F. Lee, *Nat. Commun.* **2016**, *7*, 13544.
- [40] J. R. Kremer, D. N. Mastronarde, J. R. McIntosh, *J. Struct. Biol.* **1996**, *116*, 71–76.
- [41] M. Chen, W. Dai, S. Y. Sun, D. Jonasch, C. Y. He, M. F. Schmid, W. Chiu, S. J. Ludtke, *Nat. Methods* **2017**, *14*, 983–985.
- [42] E. F. Pettersen, T. D. Goddard, C. C. Huang, G. S. Couch, D. M. Greenblatt, E. C. Meng, T. E. Ferrin, *J. Comput. Chem.* **2004**, *25*, 1605–1612.
- [43] X. Qu, D. Wu, L. Mets, N. F. Scherer, *Proc. Natl. Acad. Sci. USA* **2004**, *101*, 11298–11303.
- [44] R. Kaufmann, P. Schellenberger, E. Seiradake, I. M. Dobbie, E. Y. Jones, I. Davis, C. Hagen, K. Grünewald, *Nano Lett.* **2014**, *14*, 4171–4175.
- [45] M. Ovesný, P. Křížek, J. Borkovec, Z. Švondrych, G. M. Hagen, *Bioinformatics* **2014**, *30*, 2389–2390.
- [46] I. Y. Eremchev, M. Y. Eremchev, A. V. Naumov, *Phys.-Usp.* **2019**, *62*, 294–303.
- [47] H. Htoon, S. A. Crooker, M. Furis, S. Jeong, A. L. Efros, V. I. Klimov, *Phys. Rev. Lett.* **2009**, *102*, 017402.
- [48] L. Biadala, Y. Louyer, P. Tamarat, B. Lounis, *Phys. Rev. Lett.* **2010**, *105*, 157402.
- [49] V. D. Kulakovskii, G. Bacher, R. Weigand, T. Kümmell, A. Forchel, E. Borovitskaya, K. Leonardi, D. Hommel, *Phys. Rev. Lett.* **1999**, *82*, 1780–1783.
- [50] M. Nirmal, D. J. Norris, M. Kuno, M. G. Bawendi, *Phys. Rev. Lett.* **1995**, *75*, 3728–3731.
- [51] C. Wang, B. L. Wehrenberg, C. Y. Woo, P. Guyot-Sionnest, *J. Phys. Chem. B* **2004**, *108*, 9027–9031.

Manuscript received: February 24, 2020

Accepted manuscript online: April 24, 2020

Version of record online: May 11, 2020